Journal of Power Sources 623 (2024) 235428

Contents lists available at ScienceDirect

Journal of Power Sources

journal homepage: www.elsevier.com/locate/jpowsour

Non-equilibrium thermal models of lithium batteries

Xiaoyu Yang [a], Weiyu Li [b], Kimoon Um [c], Daniel M. Tartakovsky [a,*]

[a] Department of Energy Science and Engineering, Stanford University, 537 Panama Mall, Stanford, CA, 94305, USA
[b] Department of Mechanical Engineering, University of Wisconsin, 1513 University Ave, Madison, WI, 53706, USA
[c] Research & Development Division, Hyundai Motor Group, Gyeonggi-do, 16082, Republic of Korea

GRAPHICAL ABSTRACT

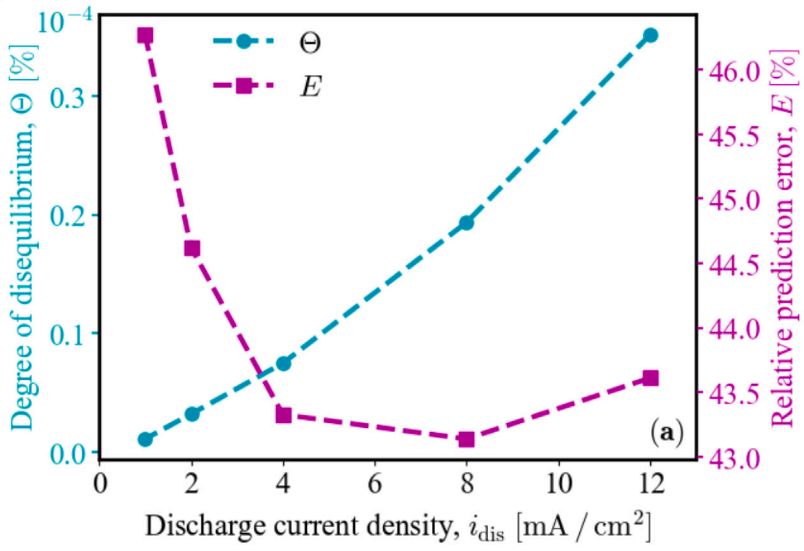

The degree of disequilibrium Θ increases with C-rate, leading to significant relative temperature-prediction error E.

HIGHLIGHTS

- Our non-equilibrium model accounts for temperature variability in active material.
- Thermal gradients in solid phase are important at high C-rates for large grains.
- The equilibrium assumption underestimates internal temperature by up to 50%.

ARTICLE INFO

Keywords:
Non-equilibrium thermal model

ABSTRACT

Temperature fluctuations impact battery performance, safety, and health. Industry-standard cell-level models of these phenomena ignore thermal gradients within the electrodes' active material, i.e., assume the latter

---

* Corresponding author.
E-mail addresses: kimoon.um@hyundai.com (K. Um), tartakovsky@stanford.edu (D.M. Tartakovsky).

https://doi.org/10.1016/j.jpowsour.2024.235428
Received 20 June 2024; Received in revised form 26 August 2024; Accepted 9 September 2024

Lithium batteries
Large thermal gradient
High C-rates
Large particles

to be in "thermal equilibrium". We present a "non-equilibrium" thermal model that explicitly accounts for spatial variability of temperature with the active material (and the carbon-binder domain). We investigate the conditions, expressed in terms of the heat-generation rate and the thermal properties of a cell's liquid (electrolyte) and solid (active material and CBD) phases, under which the thermal equilibrium assumption breaks down and our model should be used instead. The differences between these two thermal models are investigated further by coupling them with an industry-standard electrochemical model. The resulting thermal–electrochemical model demonstrates the importance of thermal gradients within the active material at high C-rates (discharge current densities) and for large grain sizes. Under these conditions, the equilibrium assumption underestimates internal temperature by as much as 50%. These two thermal models are then applied to a commercial NMC battery with multiple units. Our non-equilibrium model predicts the battery surface temperature that is in good agreement with measurements, while the equilibrium model underestimates the observed temperature.

1. Introduction

Core temperature of a battery affects its overall performance, operational safety, and ageing. A plethora of physico-chemical processes affecting this temperature include internal heat generation and heat exchange with the ambient environment. Adverse consequences of heat buildup in the battery are electrolyte decomposition and thermal runaway [1]. These processes are heterogeneous, because of the pronounced spatial variability of internal temperature [2] and correspondingly large thermal gradients [3].

Direct in situ measurements of internal temperature require thermocouple insertion [4], which is impractical at scale and yields a local measurement rather than a spatial distribution. These considerations put a premium on indirect measurements, which infer core temperature from readily observable quantities such as surface temperature [5], voltage phase shift in response to a sinusoidal current [6], or electrochemical impedance of the cell [7]. A mapping of these observables onto core temperature requires a quantitative descriptor of heat generation and transfer within the cell [8], i.e., a thermal model. Other uses of thermal models include battery health monitoring [9] and system-level thermal management [10].

Practical demands of these and other use cases drive the selection of an appropriate thermal model. While "lumped-parameter" or "energy-balance" models, e.g., [11,12], are appropriate for battery management systems, cell design and battery-health predictions might require spatially distributed models, e.g., [13]. The latter have the form of coupled partial–differential equations (PDEs), which encapsulate relevant electrochemical, thermal, and mechanical conservation laws and enable one to predict the spatiotemporal evolution of the state variables (ion concentration, voltage, temperature, etc.).

At the continuum-scale (cell-level), the electrochemical component is usually provided by the Doyle–Fuller–Newman (DFN) model [14] or its multiple variants collectively known as pseudo-two-dimensional (P2D) models [15–17]. These models account for distinct electrochemical properties of the liquid and solid phases of a cell and, to various degrees of fidelity, for electrochemical exchange at the interfaces between the two phases [18]. That is in marked contrast with the thermal component of the overall simulation, which routinely assumes the temperature of the solid and liquid phases within a representative elementary to be the same, and relies on a one-dimensional (1D) heat conduction equation [19–21] to describe the spatiotemporal evolution of this temperature in the through-cell direction. We refer to such descriptors as equilibrium thermal models.

We posit that the electrochemical–thermal models [19,20,22–24] comprising a P2D electrochemical module and a 1D thermal module contain internal contradictions. Their veracity rests on the validity of the thermal equilibrium assumption according to which temperature throughout the solid phase (active material and surrounding carbon-binder domain or CBD) is uniform. A goal of this study is to develop a new P2D non-equilibrium thermal model, which obviates the need for this assumption, and to use this model to identify conditions under which the equilibrium assumption is valid.

In the spirit of P2D electrochemical models [14–17], our thermal model explicitly differentiates between the liquid (electrolyte) and solid (active material and CBD) phases; it relies on a 1D (in the through-cell direction) representation of the former, while treating the latter as a collection of non-overlapping spheres with spatially varying temperature fields. The model accounts for heat generation due to Ohmic heat in the electrolyte and active particles, heat of chemical reaction, and heat due to entropy change at the particles' surface. When combined with the DFN model, our non-equilibrium thermal model provides a unified electrochemical–thermal representation of Li-ion batteries (LIBs).

2. Thermal models

Consider a LIB of length L. The outer surface of the negative electrode with length L_{neg} is placed at $x = 0$, the separator with length L_{sep} occupies the interval $L_{\mathrm{neg}} \leq x < L_{\mathrm{neg}} + L_{\mathrm{sep}}$, and the positive electrode with length L_{pos} resides in $L_{\mathrm{neg}} + L_{\mathrm{sep}} \leq x < L$, such that $L_{\mathrm{neg}} + L_{\mathrm{sep}} + L_{\mathrm{pos}} = L$. In a thermal model, the electrolyte and solid phase of the LIB are characterized by their respective densities, ρ_{e} and ρ_{s}, thermal conductivities, λ_{e} and λ_{s}, and heat capacities, c_{e} and c_{s}. The quantities ρ_{s}, λ_{s}, and c_{s} might be characteristics of either the active material alone or a mixture of the active material and CBD [25]. The electrodes and separator of the LIB have different porosity ω, i.e., the latter is a piecewise-constant function, $\omega(x)$, along the LIB length ($0 \leq x \leq L$).

The effective thermal conductivities of the electrolyte and solid phase in the porous electrodes, $\lambda^{\mathrm{e}}_{\mathrm{eff}}$ and $\lambda^{\mathrm{s}}_{\mathrm{eff}}$, are estimated via the empirical Bruggeman relation [26]

$$\lambda_{\mathrm{e}}^{\mathrm{eff}} = \omega^{b_{\mathrm{e}}} \lambda_{\mathrm{e}} \quad \text{and} \quad \lambda_{\mathrm{s}}^{\mathrm{eff}} = (1-\omega)^{b_{\mathrm{s}}} \lambda_{\mathrm{s}}, \tag{1}$$

where b_{e} and b_{s} are the Bruggeman exponents, which are often set to 1.5 [17]. These derived quantities are averages over a representative elementary volume (REV), which is treated as a point, x, in the continuum-scale models. Among several electrochemical parameters subjected to the same treatment are the ionic conductivity of the electrolyte, K_{e}, and the electronic conductivity of the solid phase, σ_{s}, whose effective counterpart in porous media are given by the Bruggeman relations [27,28]

$$K_{\mathrm{e}}^{\mathrm{eff}} = \omega^{b_{\mathrm{e}}} K_{\mathrm{e}} \quad \text{and} \quad \sigma_{\mathrm{s}}^{\mathrm{eff}} = (1-\omega)^{b_{\mathrm{s}}} \sigma_{\mathrm{s}}. \tag{2}$$

2.1. Local thermal equilibrium models

Current state-of-the-art predictions of the overall thermal behavior of LIBs rely on either zero- or one-dimensional local equilibrium thermal models. Zero-dimensional (lumped-parameter) models consider an entire cell to be in thermal equilibrium, treating the cell as a point [11,12]. One-dimensional models [19,21] differentiate between the LIB components – negative and positive current collectors, electrodes and separator – and assume the local thermal equilibrium between the liquid and solid phases within respective REVs of the porous electrodes and separator, i.e., assume local temperatures of the electrolyte (T_{e}) and solid phase (T_s) to be equal, $T_\mathrm{e}(x,t) = T_\mathrm{s}(x,t) \equiv T(x,t)$. The spatiotemporal evolution of $T(x,t)$ in the through-cell direction is described by a 1D heat conduction equation [29]

$$\rho c \frac{\partial T}{\partial t} = \frac{\partial}{\partial x}\left(\lambda \frac{\partial T}{\partial x}\right) + Q_\mathrm{tot}, \qquad x \in (0, L), \quad t > 0. \tag{3a}$$

This model is parameterized by the lumped density and lumped specific heat capacity [25],

$$\rho = \omega\rho_\mathrm{e} + (1-\omega)\rho_\mathrm{s} \quad \text{and} \quad c = \frac{\omega\rho_\mathrm{e}c_\mathrm{e} + (1-\omega)\rho_\mathrm{s}c_\mathrm{s}}{\omega\rho_\mathrm{e} + (1-\omega)\rho_\mathrm{s}}, \tag{3b}$$

respectively; and by the lumped effective thermal conductivity [26],

$$\lambda(x) = \begin{cases} \lambda_\mathrm{e}^\mathrm{eff} + \lambda_\mathrm{s}^\mathrm{eff} & x \in \Omega_\mathrm{ele} \\ \lambda_\mathrm{sep} & \text{otherwise.} \end{cases} \tag{3c}$$

Instead of using these formulae, one can determine these parameters experimentally [30,31].

The source function $Q_\mathrm{tot}(x,t)$ represents the total heat generated at space–time point (x,t),

$$Q_\mathrm{tot} = Q_\mathrm{ohm}^\mathrm{e} + Q_\mathrm{ohm}^\mathrm{s} + A_\mathrm{rs}Q_\mathrm{ent} + A_\mathrm{rs}Q_\mathrm{rea}. \tag{4a}$$

The irreversible (volumetric) Ohmic heat generation in the electrolyte, $Q_\mathrm{ohm}^\mathrm{e}(x,t)$, and solid phase, $Q_\mathrm{ohm}^\mathrm{s}(x,t)$, is induced by the ionic resistance under the gradients of electric potentials in the electrolyte (φ_e) and solid material (φ_s) and Li$^+$ concentration in the electrolyte (C_e):

$$Q_\mathrm{ohm}^\mathrm{e} = K_\mathrm{e}^\mathrm{eff}\frac{\partial \varphi_\mathrm{e}}{\partial x}\left(\frac{\partial \varphi_\mathrm{e}}{\partial x} + \kappa_\mathrm{e}\frac{\partial \ln C_\mathrm{e}}{\partial x}\right), \qquad Q_\mathrm{ohm}^\mathrm{s} = \sigma_\mathrm{s}^\mathrm{eff}\left(\frac{\partial \varphi_\mathrm{s}}{\partial x}\right)^2, \tag{4b}$$

where $\kappa_\mathrm{e} = 2\mathcal{R}T\alpha(t^+ - 1)/F$; $\mathcal{R}$ and F are the gas and Faraday constants, respectively; α is the activity coefficient; and t^+ is the cation transference number (a given function of C_e). The specific reactive surface area $A_\mathrm{rs} = 3(1-\omega)/R$ is a function of porosity ω and solid particle radius R. The entropic (Q_ent) and reaction (Q_rea) heat generation is associated with ion intercalation in porous electrodes. Both vary linearly with the intercalation current density $J(x,t)$,

$$Q_\mathrm{ent} = JT\frac{\partial U(\xi, T)}{\partial T}, \qquad Q_\mathrm{rea} = J\eta. \tag{4c}$$

Here, $\eta(x,t) = \phi_\mathrm{s} - \phi_\mathrm{e} - U$ is the overpotential; and the open circuit potential U depends on both the temperature $T(x,t)$ and the Li filling fraction $\xi(x,t) = C_\mathrm{s}(R,t;x)/C_\mathrm{s}^\mathrm{max}$ that is defined as the ratio between the Li concentration at the solid particle surface, $C_\mathrm{s}(R,t;x)$, and the maximum Li concentration that can be stored in the active particle, $C_\mathrm{s}^\mathrm{max}$. According to the Butler–Volmer equation,

$$J = 2Fk_0C_\mathrm{s}^\mathrm{max}\sqrt{C_\mathrm{e}\xi(1-\xi)}\sinh\left(\frac{F\eta}{2\mathcal{R}T}\right), \tag{4d}$$

where k_0 is the reaction rate constant. The heat generation terms in Eq. (4) depend on the electric potential and the Li concentration in the liquid electrolyte and solid phase, $\phi_\mathrm{e}(x,t)$, $C_\mathrm{e}(x,t)$, $\phi_\mathrm{s}(x,t)$, and $C_\mathrm{s}(R;x,t)$. These state variables are obtained by solving an electrochemical P2D model, such as the DFN model [14].

If the battery's initial temperature is T_in and the ambient temperature is T_amb, Eqs. (3) and (4) are solved subject to the initial condition

$$T(x,0) = T_\mathrm{in}, \qquad x \in (0, L), \tag{5a}$$

and the boundary conditions

$$-\lambda\frac{\partial T}{\partial x}(0,t) = h_\mathrm{neg}[T_\mathrm{amb} - T(0,t)], \qquad -\lambda\frac{\partial T}{\partial x}(L,t) = h_\mathrm{pos}[T(L,t) - T_\mathrm{amb}], \tag{5b}$$

where h_neg and h_pos are the heat transfer coefficients at the outer surfaces of the negative and positive electrodes, respectively. These boundary conditions represent convective heat transfer between the battery's outer surfaces ($x = 0$ and L) and the ambient environment. When the two ends of the LIB are exposed to the same environmental conditions, the situation considered in the numerical experiments below, $h_\mathrm{neg} = h_\mathrm{pos} = h$.

The local thermal equilibrium assumption, which undergirds this thermal model, postulates the absence of interfacial heat transfer between the electrolyte and the solid phase. This assumption is not universally valid. First, the rates of Ohmic heat generation in the two phases might differ due to differences in the ionic conductivities and electric fields. For instance, the volumetric Ohmic heat generation in the liquid electrolyte can be an order of magnitude higher than that within the cathode particles [32]. Second, there can be significant interfacial entropic and reactive heat generation, particularly under high C-rates. Third, through-cell conductive heat enters the two phases differently due to variations in their thermal properties [30]. These conditions, coupled with poor effective thermal diffusivity of electrodes, are likely to induce substantial imbalance between the temperatures of the electrolyte and the solid. In the following, we formulate a thermal model that is free of the local equilibrium assumption and incorporates interfacial heat generation.

2.2. *Local thermal non-equilibrium model*

We formulate a new thermal model of LIBs in a manner consistent with the standard DFN model [14], treating the porous electrodes and separator as 1D continuum media and representing the solid phase as a collection of non-overlapping spheres [17]. Our model neglects heat conduction in current collectors due to their small thermal resistances; this phenomenon can be readily incorporated in our framework, as needed. The continuum-scale spatiotemporal evolution of the electrolyte temperature, $T_\mathrm{e}(x,t)$, in the electrodes, $\Omega_\mathrm{ele} = (0, L_\mathrm{neg}) \cup (L - L_\mathrm{pos}, L)$, is described by a 1D heat conduction equation

$$\omega\rho_\mathrm{e}c_\mathrm{e}\frac{\partial T_\mathrm{e}}{\partial t} = \frac{\partial}{\partial x}\left(\lambda_\mathrm{e}^\mathrm{eff}\frac{\partial T_\mathrm{e}}{\partial x}\right) + Q_\mathrm{ohm}^\mathrm{e} + A_\mathrm{rs}Q_\mathrm{int}^\mathrm{e}, \qquad x \in \Omega_\mathrm{ele}, \quad t > 0. \tag{6}$$

The Ohmic heat generation in the electrolyte, $Q_\mathrm{ohm}^\mathrm{e}$, is defined by Eq. (4b); the interfacial heat flux entering the electrolyte, $Q_\mathrm{int}^\mathrm{e}$, satisfies a balance relation [25],

$$Q_\mathrm{int}^\mathrm{e} - Q_\mathrm{int}^\mathrm{s} = Q_\mathrm{ent} + Q_\mathrm{rea}, \tag{7a}$$

in which the entropic, Q_ent, and reaction, Q_rea, heat production rates are given by Eq. (4c); and the normal component of the interfacial heat flux leaving the spherical particles, $Q_\mathrm{int}^\mathrm{s}$, obtained from the Fourier law written in the spherical coordinates,

$$Q_\mathrm{int}^\mathrm{s} = -\lambda_\mathrm{s}\frac{\partial T_\mathrm{s}}{\partial r} \quad \text{at} \quad r = R. \tag{7b}$$

Assuming the radial symmetry, we derive in the Appendix an equation for temperature in the solid particles, $T_\mathrm{s}(r,t;x)$:

$$\rho_\mathrm{s}c_\mathrm{s}\frac{\partial T_\mathrm{s}}{\partial t} = \frac{1}{r^2}\frac{\partial}{\partial r}\left(\lambda_\mathrm{s}r^2\frac{\partial T_\mathrm{s}}{\partial r}\right) + \frac{Q_\mathrm{ohm}^\mathrm{s}}{1-\omega} + \frac{1}{1-\omega}\frac{\partial}{\partial x}\left(\lambda_\mathrm{s}^\mathrm{eff}\frac{\partial T_\mathrm{e}}{\partial x}\right), \qquad 0 < r < R, \tag{8}$$

where the Ohmic heat generation in the solid phase, $Q_\mathrm{ohm}^\mathrm{s}$, is given by Eq. (4b).

Like Eq. (6), the equation above is defined for the porous electrodes, $x \in \Omega_\mathrm{ele}$. The separator, $x \in \Omega_\mathrm{sep} = (L_\mathrm{neg}, L - L_\mathrm{pos})$, is treated as a 1D continuum medium. Its temperature, $T_\mathrm{sep}(x,t)$, satisfies Eq. (3a) on the interval $x \in \Omega_\mathrm{sep}$. At the electrode/separator interfaces $x = L_\mathrm{neg}$ and $x = L - L_\mathrm{pos}$, the solutions of these three heat-conduction equations satisfy continuity conditions

$$T_\mathrm{e} = T, \qquad -(\lambda_\mathrm{e}^\mathrm{eff} + \lambda_\mathrm{s}^\mathrm{eff})\frac{\partial T_\mathrm{e}}{\partial x} = -\lambda_\mathrm{sep}\frac{\partial T}{\partial x}. \tag{9a}$$

Similar to Eq. (5), the boundary conditions at the LIB's bounding surfaces, $x = 0$ and $x = L$, are

$$-\lambda\frac{\partial T_\mathrm{e}}{\partial x}(0,t) = h[T_\mathrm{amb} - T_\mathrm{e}(0,t)], \qquad -\lambda\frac{\partial T_\mathrm{e}}{\partial x}(L,t) = h[T_\mathrm{e}(L,t) - T_\mathrm{amb}]. \tag{9b}$$

At any point $x \in \Omega_{ele}$, the surface temperature of solid particles, $T_s(R,t;x)$, aligns with the surrounding electrolyte temperature, $T_e(x,t)$, when the thermal contact resistance is neglected [33]. Combined with the condition that $T_s(0,t;x)$ must remain finite at all times, this gives rise to boundary conditions for Eq. (8),

$$\frac{\partial T_s}{\partial r}(0,t;x) = 0, \quad T_s(R,t;x) = T_e(x,t). \tag{9c}$$

The LIB's initial temperature is consistent with Eq. (5a),

$$\begin{aligned} &T_e(x,0) = T_s(r,0;x) = T_{in}, \quad x \in \Omega_{ele} \\ &T_{sep}(x,0) = T_{in}, \quad x \in \Omega_{sep}. \end{aligned} \tag{9d}$$

To gain a physical insight into the effective representation of heat transfer in the porous electrodes provided by Eqs. (6) and (8) we compute the heat balance for the spherical particle during the time interval $(0,t)$. Integrating Eq. (8) over time and particle volume, integrating Eq. (6) over time, and combining the two yields an expression for the difference between the electrolyte temperature $T_e(x,t)$ and the average solid-phase temperature $\bar{T}_s(x,t)$:

$$T_e - \bar{T}_s = \mathcal{E}_{ohm} + \mathcal{E}_{int} + \mathcal{E}_{con}. \tag{10a}$$

This difference stems from the discrepancy between the Ohmic heat generation in the liquid electrolyte and solid particle,

$$\mathcal{E}_{ohm} = \int_0^t (\gamma_e Q^e_{ohm} - \gamma_s Q^s_{ohm}) d\tau, \tag{10b}$$

between the interfacial heat fluxes due to the entropic and reaction heat generation,

$$\mathcal{E}_{int} = A_{rs} \int_0^t (\gamma_e Q^e_{int} - \gamma_s Q^s_{int}) d\tau, \tag{10c}$$

and between the heat conduction caused by the variation of the physical and thermal properties of the two phases,

$$\mathcal{E}_{con} = \int_0^t \left[\gamma_e \frac{\partial}{\partial x}\left(\lambda^{eff}_e \frac{\partial T_e}{\partial x}\right) - \gamma_s \frac{\partial}{\partial x}\left(\lambda^{eff}_s \frac{\partial T_e}{\partial x}\right) \right] d\tau. \tag{10d}$$

Here, $\bar{T}^s = (4\pi/V_s)\int_0^R T_s r^2 dr$, $V_s = 4\pi R^3/3$ is the particle volume, $\gamma_e = 1/(\omega \rho_e c_e)$, and $\gamma_s = 1/[(1-\omega)\rho_s c_s]$. Local thermal equilibrium requires $T_e(x,t) = \bar{T}_s(x,t)$, which implies the absence of temperature gradients inside the solid particles, i.e., $T_s(r,t;x) = \bar{T}_s(x,t)$.[1] Eq. (10) identifies three sources of local thermal disequilibrium, which stem from the contrast in the electrochemical and thermal properties of the electrolyte and solid phase.

These considerations suggest that our non-equilibrium thermal model is a generalization of the currently used equilibrium ones. Physicochemical conditions under which our model reduces to the latter are investigated below via a series of numerical experiments.

3. Electrochemical–thermal models

Both equilibrium and non-equilibrium thermal models described above are strongly coupled with the electrochemical model [17] through the interdependence of the battery temperature and the other state variables, $C_e(x,t)$, $C_s(R;x,t)$, $\phi_e(x,t)$, and $\phi_s(x,t)$. To compute these, we couple our alternative thermal models with the DFN model implemented in `PyBaMM`. (The latter is a Python-based battery simulator widely used in the field, https://pybamm.org.) Every temperature-dependent parameter in the DFN model, $\mathcal{P}$, (i.e., electrode diffusivity, exchange current density, electrolyte diffusivity and conductivity) follows the Arrhenius equation,

$$\mathcal{P}(T) = \mathcal{P}_{ref} \exp\left[\frac{E}{R}\left(\frac{1}{T_{ref}} - \frac{1}{T}\right)\right], \tag{11}$$

where $\mathcal{P}_{ref}$ is the value of the corresponding parameter $\mathcal{P}$ at reference temperature T_{ref}, and E is the activation energy.

The local equilibrium model is part of `PyBaMM`. Its non-equilibrium counterpart is solved via the finite-volume method with a fully coupled and fully implicit scheme for time integration. The research code is written in Python. The porous electrodes, the separator, and the solid particles are each discretized with uniform grids consisting of 40 elements.

4. Numerical experiments

Although our local thermal non-equilibrium model is applicable to both Li-metal and Li-ion batteries, we demonstrate it on a specific LIB structure with porous electrodes [34], which comprises graphite on the anode, Li(NiMnCo)O2 on the cathode, and an EC/EMC mixture with $LiPF_6$ for electrolyte. Its material properties and operation conditions are summarized in Table 1. In the first numerical experiment, to verify the effectiveness of the non-equilibrium thermal model, we enforce a local thermal equilibrium condition by selecting a heat generation distribution and electrode properties. In the second set of experiments, we couple the thermal model with the DFN model and demonstrate our model's performance on the four LIBs in Table 1.

4.1. Verification of non-equilibrium model

To verify the self-consistency of the local thermal non-equilibrium model, we compare its predictions with those of the local thermal equilibrium model under conditions of thermal equilibrium. According to Eq. (10), the attainment of local thermal equilibrium depends on heat generation and heat conduction within a cell. We consider a local equilibrium condition governed by uniform heat generation distribution for a battery with the same structure as LIB 1 in Table 1. To eliminate the contribution of spatially varying through-cell conduction, i.e., to enforce $\mathcal{E}_{con} = 0$, the physical and thermal properties (density, specific heat capacity, thermal conductivity) of the solid phase and the electrolyte are assumed to be the same and porosity is set to $\omega = 0.5$. Under these conditions, Eq. (10) reduces to $T_e - \bar{T}_s = \mathcal{E}_{ohm} + \mathcal{E}_{int}$. The local thermal equilibrium, $T_e = \bar{T}_s$, signifies the absence of the interfacial heat flux between the electrolyte and the solid phase; the energy balance equation (7a) translates this condition into $Q^s_{int} = 0$ and $Q^e_{int} = Q_{ent} + Q_{rea}$. Combining these relations with Eqs. (10b) and (10c), we obtain an energy balance for the local thermal equilibrium:

$$Q^e_{ohm} + A_{rs}(Q_{ent} + Q_{rea}) = (\gamma_s/\gamma_e) Q^s_{ohm}. \tag{12}$$

This relation states that porous electrodes are in local thermal equilibrium when the increase of electrolyte temperature due to Ohmic and interfacial heat generation in the electrolyte matches the increase of solid-phase temperature caused by Ohmic heat generation in the solid phase.

To satisfy Eq. (12), we set $Q^e_{ohm} = Q^s_{ohm} = 10^6$ J/m^3 in the negative electrode, and the remaining heat sources to zero. In accordance with the theoretical considerations above, the temperature of the solid particles, T_s, predicted by our non-equilibrium model is indeed uniform (Fig. A.1 in the Appendix); the lack of temperature gradient translates into zero interfacial heat flux between the electrolyte and the solid phase. The temperature increases with time, reflecting the heat accumulation within the cell. In this regime, predictions of the equilibrium and non-equilibrium models coincide (Fig. 1), as they should.

Having verified that predictions of the non-equilibrium model coincide with those of the equilibrium model under the artificially imposed thermal equilibrium condition, we proceed to investigate the impact of material properties and operation conditions on internal temperature and on the validity of the equilibrium approximation. Since in-cell temperature variability is the focus of battery thermal modeling, we define the degree of disequilibrium as a measure of the

---

[1] This result stems from the maximum principle according to which the function $T_s(r,\cdot)$–a solution of the heat conduction equation with the spatially homogeneous heat sources, Eq. (8)–is monotonic [25].

Table 1

Material properties and operation conditions of four generic LIBs. The parameter values indicated by † are for a standard electrolyte (BASF, LP50) [35], by ‡ are from the Ecker2015 parameter set in PyBaMM, and by ♭ are calculated via Eqs. (1) or (3b) using the lumped electrode parameter values in the Ecker2015 parameter set.

Negative electrode's thickness, L_{neg} [10^{-5}m]				7.4 ‡
Positive electrode's thickness, L_{pos} [10^{-5}m]				5.4 ‡
Separator thickness, L_{sep} [10^{-5}m]				2.0 ‡
Positive particle radius, R_{pos} [10^{-6}m]				6.5 ‡
Electrolyte density, ρ_{e} [kg/m^3]				1249 †
Negative electrode solid density, $\rho_{\text{s,neg}}$ [kg/m^3]				1705 ♭
Positive electrode solid density, $\rho_{\text{s,pos}}$ [kg/m^3]				3587 ♭
Separator density, ρ_{sep} [kg/m^3]				1017 ‡
Electrolyte specific heat capacity, c_{e} [J/(kgK)]				1642 †
Negative electrode solid specific heat capacity, $c_{\text{s,neg}}$ [J/(kgK)]				1363 ♭
Positive electrode solid specific heat capacity, $c_{\text{s,pos}}$ [J/(kgK)]				1216 ♭
Separator specific heat capacity, c_{sep} [J/(kgK)]				1978 ‡
Electrolyte thermal conductivity, λ_{e} [W/(mK)]				0.18 †
Positive electrode solid thermal conductivity, $\lambda_{\text{s,pos}}$ [W/(mK)]				1.71 ♭
Separator thermal conductivity, λ_{sep} [W/(mK)]				0.34 ‡
Negative electrode porosity, ω_{neg} [−]				0.329 ‡
Positive electrode porosity, ω_{pos} [−]				0.296 ‡
Ambient temperature, T_{amb} [°C]				25
Initial temperature, T_{in} [°C]				25
Discharge current density, i_{dis} [mA/cm^2]				[1, 12]
	LIB1	LIB2	LIB3	LIB4
Negative electrode solid thermal conductivity, $\lambda_{\text{s,neg}}$ [W/(mK)]	2.81 ♭	0.0281	2.81	2.81
Negative particle radius, R_{neg} [10^{-5}m]	1.37 ‡	1.37	0.25, 1.37	1.37
Heat transfer coefficient, h [W/(m^{2}K)]	0	0	0	100

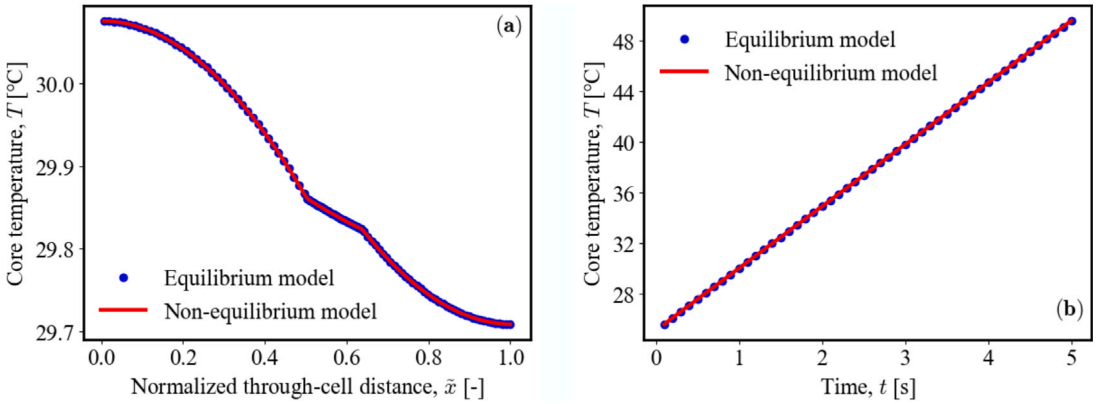

Fig. 1. Core temperature of a LIB in local thermal equilibrium, alternatively predicted with the equilibrium and non-equilibrium models. **(a)** Through-cell temperature profile $T(x,t)$ at time $t = 1$ s, plotted against the normalized coordinate $\tilde{x} = x/L$. **(b)** Temporal evolution of $T(x,t)$ at the center of the negative electrode, $\tilde{x} = 0.25$.

relative magnitude of the local thermal disequilibrium relative to the cell temperature increase under different operations (e.g., discharge current density, operation temperature, etc.). We quantify the degree of thermal disequilibrium in terms of a relative average temperature difference between the two phases,

$$\Theta(t) = \frac{1}{\|\Omega_{\text{ele}}\|\, t} \int_{\Omega_{\text{ele}}} \int_0^t \frac{T_{\text{e}}(x,t) - \bar{T}_{\text{s}}(t;x)}{|T_{\text{e}}(x,t) - T_{\text{e}}(x,0)|} \mathrm{d}\tau \mathrm{d}x. \tag{13}$$

The value $\Theta = 0$ represents local thermal equilibrium, while a positive (negative) value of Θ corresponds to the influx (outflow) of heat into (from) the solid phase from (into) the electrolyte. The equilibrium and non-equilibrium thermal models are coupled with the electrochemical DFN model to predict internal temperature of a LIB during discharge. The predictions of the resulting two models are denoted by $T_{\text{1D}}(x,t)$ and $T_{\text{P2D}}(x,t) = T_{\text{e}}(x,t)$, respectively. Since the equilibrium model is derived from the non-equilibrium one, $T_{\text{1D}}(x,t)$ is an approximation of $T_{\text{P2D}}(x,t)$. The error of this approximation is reported in terms of the relative average temperature discrepancy, $E(t)$,

$$E(t) = \frac{1}{\|\Omega_{\text{ele}}\|\, t} \int_{\Omega_{\text{ele}}} \int_0^t \frac{T_{\text{P2D}}(x,t) - T_{\text{1D}}(x,t)}{|T_{\text{1D}}(x,t) - T_{\text{1D}}(x,0)|} \mathrm{d}\tau \mathrm{d}x. \tag{14}$$

4.2. *Influence of thermal conductivity of solid phase*

Thermal conductivity of the solid phase, λ_{s}, impacts the rate with which the temperature equilibrates and, hence, is expected to affect the validity of the equilibrium assumption. The dependence of Θ on thermal conductivity of the negative electrode in LIB 2 under discharge confirms this assessment (Fig. 2a). The system shows larger local thermal disequilibrium under faster discharge ($i_{\text{dis}} = 12$ mA/cm^2), which induces more pronounced spatial variability of heat generation in porous electrodes. The magnitude of local thermal non-equilibrium decreases as $\lambda_{\text{s,neg}}$ increases, enhancing heat transfer at the electrolyte–solid interface and, hence, smoothing out the heat-generation differences between the two phases. While the degree of disequilibrium Θ is very small (on the order of 10^{-3}%), it has a large impact on the error introduced by the equilibrium assumption, $E \sim 44\%$ (Fig. 2b). That is because of the highly nonlinear dependence between the state variables of the electrochemical–thermal models.

4.3. *Influence of particle size*

Both the standard P2D model and its non-equilibrium counterpart presented here deal with uniform particles. Generalization to particle-size distributions is relatively straightforward, but lies outside the scope

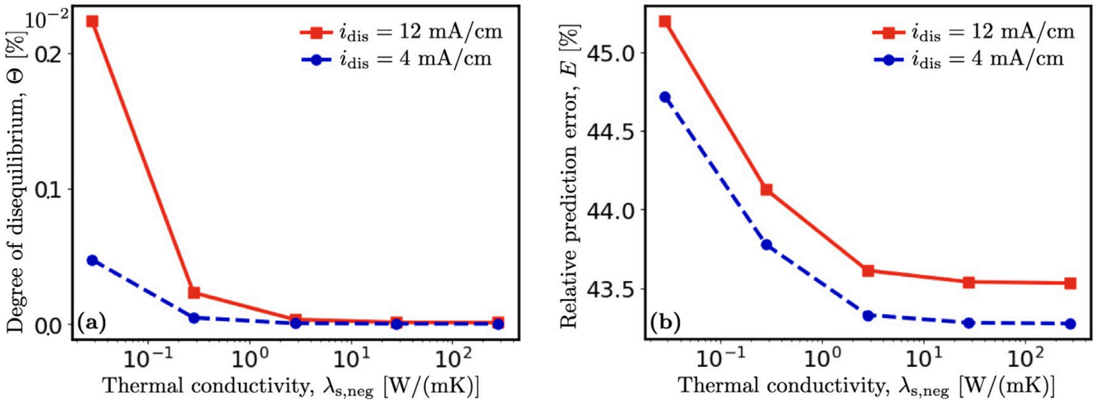

Fig. 2. Dependence of **(a)** degree of disequilibrium Θ and **(b)** relative temperature–prediction error E on thermal conductivity of the solid phase of the negative electrode, $\lambda_{\mathrm{s,neg}}$, during LIB discharge at current density $i_{\mathrm{dis}} = 12$ mA/cm^2 (solid line) and 4 mA/cm^2 (dashed line).

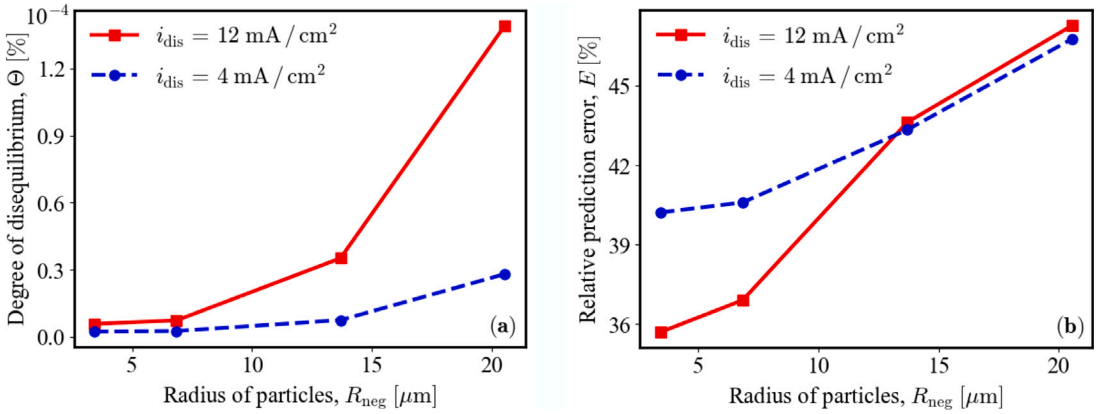

Fig. 3. Dependence of **(a)** degree of disequilibrium Θ and **(b)** relative temperature–prediction error E on the radius of particles in the negative electrode, R_{neg}, during LIB discharge at current density $i_{\mathrm{dis}} = 12$ mA/cm^2 (solid line) and 4 mA/cm^2 (dashed line).

of our study and is left for a follow-up study. The size of particles, used in the P2D models to represent the solid phase of porous electrodes, is expected to impact the veracity of the equilibrium assumption since, all other parameters being equal, the temperature in smaller particles would equilibrate faster. Fig. 3 demonstrates this phenomenon for LIB 3 discharging at current density $i_{\mathrm{dis}} = 12$ mA/cm^2 and 4 mA/cm^2. We focus on negative-electrode particles to investigate the effect of particle size; the size of positive-electrode particles is expected to have similar influence on thermal behaviors. The degree of disequilibrium Θ and the equilibrium-assumption error E both increase with the particle size. It takes the thermal conduction longer to uniformly heat larger particles, erasing the difference between the electrolyte temperature and the average temperature of the solid phase. The characteristic time for this process to occur, $\tau = R^2/\kappa$ where $\kappa = \lambda_{\mathrm{s}}/(\rho_{\mathrm{s}} c_{\mathrm{s}})$ is the thermal diffusivity, increases as the square of the particle radius R. As before, the minuscule degree of disequilibrium, $\Theta \sim 10^{-4}$%, give rise to the considerable equilibrium-assumption error, $E \sim 40$%.

The error E is global, i.e., averaged over the LIB length and time of operation t. A point-wise discrepancy between the temperature predictions of the equilibrium and non-equilibrium models of LIB 3, $T_{\mathrm{1D}}(x,t)$ and $T_{\mathrm{P2D}}(x,t)$, is shown in Fig. 4a for $x = 0.25L$ (the middle of the negative electrode) and discharge current density $i_{\mathrm{dis}} = 12$ mA/cm^2; the discharge capacity $C_{\mathrm{d}} = i_{\mathrm{dis}} t/3600$ is used in lieu of time. Both models capture an experimentally observed increase in discharge time as the particle size decreases, resulting in a larger specific area for the intercalation/deintercalation reactions [36] and faster ion diffusion through smaller particles [37]. Yet, the equilibrium model underestimates both the core temperature at point $x = 0.25L$ by as much as 20% and the discharge time by about 10%. This discrepancy increases with the particle size R, because of the enhanced local thermal disequilibrium.

4.4. Influence of heat transfer coefficient

The three LIBs studied above have no external cooling, since their heat transfer coefficient at the outer surfaces of the two electrodes is $h = 0$ (Table 1). In LIB 4, this parameter varies from $h = 0$ to 100 W/(m^{2}K). The local thermal disequilibrium, Θ, increases almost linearly with h (Fig. 5a), which stems from the increased spatial variability of thermal conduction in the solid and the electrolyte due to different material properties. The impact of the external cooling on the equilibrium-assumption error, E is nearly exponential (Fig. 5b); E increases from just below 45% for $h = 0$ to over 65% for $h = 100$ W/(m^{2}K). As to be expected, the impact of increased cooling, i.e., of larger values of h, is to reduce the internal LIB temperature and its discharge time (Fig. 4b). The equilibrium model systematically underpredicts the discharge capacity, with the error being more pronounced under poor cooling ($h = 0$).

4.5. Influence of C-rate (discharge current density)

Our previous results demonstrated that local thermal disequilibrium became more pronounced and, hence, the 1D thermal model implemented in `PyBAMM` became less accurate, as discharge current density i_{dis} increased from 4 mA/cm^2 to 12 mA/cm^2, with the corresponding three-fold increase in C-rate, i.e., the ratio of discharge current $i_{\mathrm{dis}}\mathcal{A}$ (where $\mathcal{A}$ is the cross-sectional area of the cell) to nominal cell capacity. We elaborate on this point by exhibiting the degree of thermal disequilibrium in LIB 1, and the concomitant error of the thermal-equilibrium assumption, for a range of C-rates (Fig. 6).

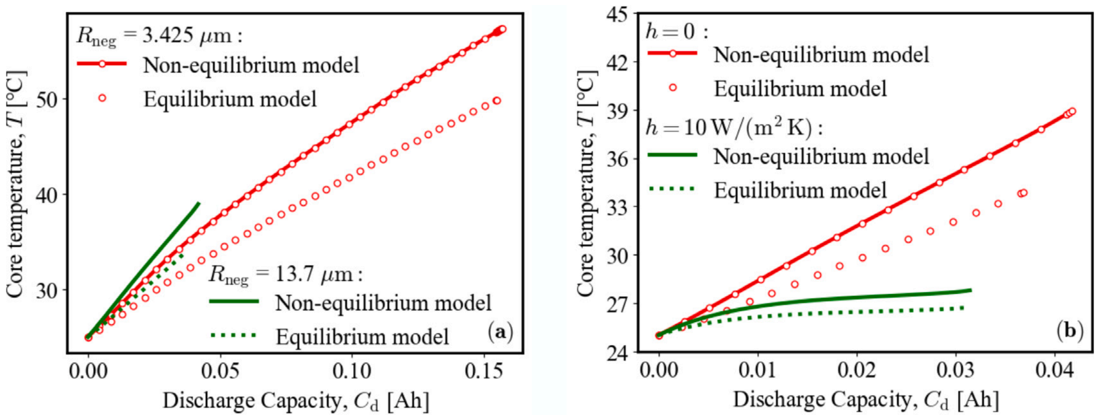

Fig. 4. Temporal evolution (expressed as discharge capacity, $C_d = i_{dis}t/3600$) of internal temperature $T(x,t)$ at the center of the negative electrode, $x = 0.25L$, for discharge current density i_{dis} = 12 mA/cm^2 and **(a)** particle radius R_{neg} = 3.425 μm (red line) and 13.7 μm (green line), and **(b)** heat transfer coefficient h = 0 (red line) and 10 W/(m^{2}K) (green line). (For interpretation of the references to color in this figure legend, the reader is referred to the web version of this article.)

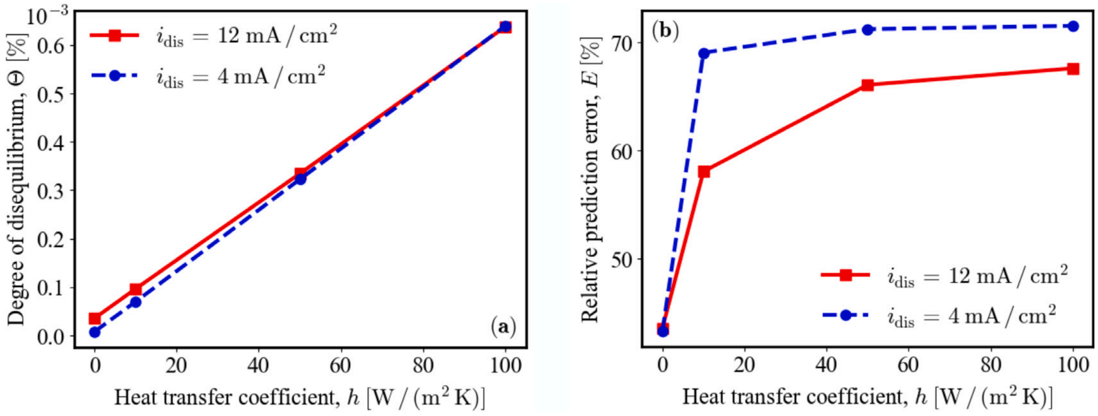

Fig. 5. Dependence of **(a)** degree of disequilibrium Θ and **(b)** relative temperature–prediction error E on heat transfer coefficient h, during LIB discharge at current density i_{dis} = 12 mA/cm^2 (solid line) and 4 mA/cm^2 (dashed line).

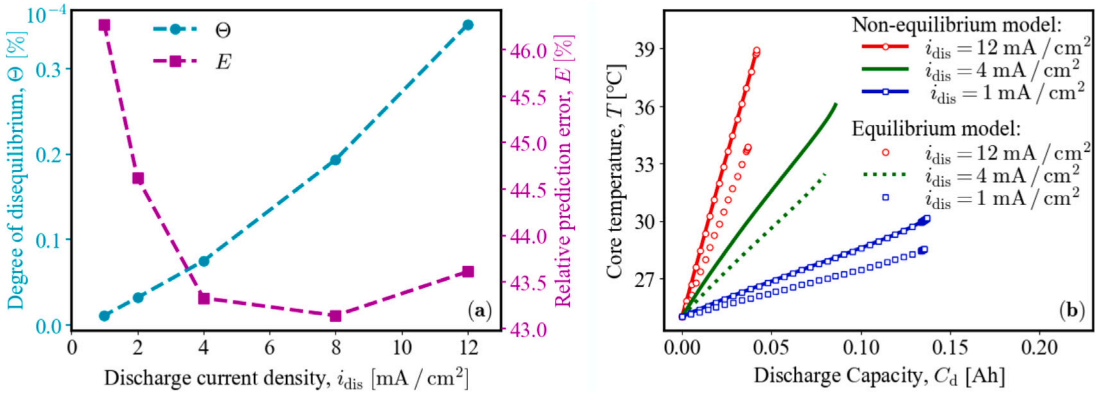

Fig. 6. **(a)** Dependence of degree of disequilibrium Θ (solid line) and relative temperature–prediction error E (dashed line) on C-rate, for LIB 1. **(b)** Temporal evolution (discharge capacity, $C_d = i_{dis}t/3600$) of internal temperature $T(x,t)$ at the center of the negative electrode ($x = 0.25L$), for current density i_{dis} = 12 mA/cm^2 and 4 mA/cm^2.

Experimental evidence [38] reveals that heat generation in a LIB increases with i_{dis} and, hence, with C-rate. This phenomenon is accompanied by a more pronounced variation in the amounts of heat generated in the electrolyte and the solid phase, especially at high C-rates for which Ohmic heat generation dominates the other modes of heat production [39]. Resistance to ion transport in the electrolyte and to electron transport in the solid phase determines Ohmic heat in the respective phases, with the ion-transport resistance being larger than the electron-transport resistance. The latter difference ensures that, as C-rate increases, Ohmic heat production in the electrolyte becomes progressively larger than its counterpart in the solid phase, accentuating the heat variability between the two phases. Since heat transfer between the two phases is limited by their thermal properties, the heat non-uniformity cannot be quickly eliminated and local thermal disequilibrium Θ is enhanced (Fig. 6a). At any C-rate, the relative average error E of over 46% cannot be ignored, even if Θ is small.

Fig. 6b shows the temporal evolution of internal temperature $T(x,t)$ in the middle of the negative electrode of LIB 1, $x = 0.25L$, for a

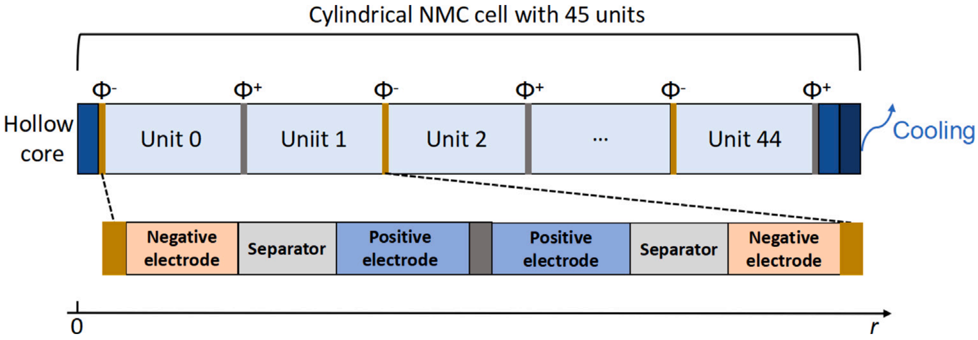

Fig. 7. Schematics of a cylindrical NMC battery.

wide range of C-rates. As C-rate increases, the prediction error of the equilibrium model becomes more pronounced due to the enhanced local thermal disequilibrium. The equilibrium model systematically underestimates the core temperature, potentially undermining the online thermal management due to, e.g., the battery capacity's decline when the battery temperature increases approximately 25 °C from the room temperature regardless of cell chemistry [40]. The non-equilibrium model predicts a longer discharge time than the equilibrium model under the same discharge current density.

5. Application to a commercial NMC battery

Commercial batteries consist of multiple cathode–separator–anode units. We extend our model to such a setting and apply it to a 5 Ah M50 21700 cylindrical cell manufactured by LG Chem (LG M50). The active materials in positive and negative electrodes are nickel-rich NMC811 and graphite–SiO_x, respectively. The cylindrical battery contains a hollow core, a spiral, a contact layer, and a casing from its center to its outer surface. The hollow core is filled with liquid electrolytes, the spiral is fabricated by rolling the double-sided electrodes and the separators, and the casing is made up of either metals, alloys, or plastics [41]. Each 360° spiral ring in the spiral can be considered as a single unit. If the revolution number is N, then the battery consists of $2N-1$ units, connected in parallel to each other [42]. A representative NMC battery has the total of 45 units (Fig. 7). Our thermal model of this cylindrical battery assumes heat flow in the axial and angular directions to be negligible [43], i.e., describes heat transfer in the radial direction, from the hollow core to the casing. Temperature within each unit is described by our electrochemical–thermal models from Section 3; these models are coupled by enforcing the temperature and heat flux continuity conditions at the interfaces between two adjacent units. An overall heat transfer coefficient [41] is set at the outer radius of the battery, and zero heat flux is set at the battery center. Our goal is to predict the temperature distribution inside the battery during its discharge, and to compare the model's prediction of the battery surface temperature to the experimental data reported in [44].

Most of the electrochemical and thermal parameters are taken directly from [45,46], respectively. The remaining seven parameters are reported in Table 2. They are computed by minimizing the root mean squared error (RSME) between the model-predicted and the measured evolution of surface temperature during 1C discharge and under 25 °C operation temperature. This task is accomplished via the particle swarm optimization algorithm in `Pymoo` [47], separately for the non-equilibrium and equilibrium P2D models.

Fig. 8 exhibits the predicted and measured battery surface temperature during 1C discharge under 25 °C and 35 °C operation temperature. Since the parameters are calibrated for 25 °C, the two models have a similarly small RMSE, indicating the two models ability to match the observations (Fig. 8, left). When the models are used in a purely predictive mode, i.e., for 35 °C to which the models are not calibrated, the non-equilibrium model is significantly more accurate than the equilibrium one (Fig. 8, right). The RMSE of the former is half that of the latter. The equilibrium model significantly underestimates the battery temperature, potentially undermining its use for thermal management.

6. Conclusions

Thermal models are routinely coupled with electrochemical models to predict the thermal–electrochemical behavior of energy storage devices, e.g., lithium batteries. The accuracy and robustness of such physicochemical models is strongly affected by their temperature-dependent electrochemical parameters, whose estimation depends in large part on the performance of the thermal component of an overall model. The industry standard in thermal modeling relies on the local thermal equilibrium assumption, which breaks down for porous electrodes with significant heat generation and contrast in the thermal diffusion between the electrolyte and the solid phase. By ignoring heat transfer between the two phases, the local thermal equilibrium model systematically underestimates a LIB's core temperature, undermining its utility for local hotspot prediction and thermal runaway prevention.

We proposed a local thermal non-equilibrium model, which falls within the realm of the pseudo-two-dimensional (P2D) modeling framework that routinely used to forecast electrochemical processes in LIBs. The solid phase in porous electrodes is described via a collection of non-overlapping spheres of identical radius, whose outer surface is in thermal equilibrium with the surrounding electrolyte. Our thermal non-equilibrium model can be seamlessly combined with any P2D electrochemical model, such as the DFN model used in this study. We conducted a series of numerical experiments with four representative LIBs to quantify the effects of cell properties (e.g., thermal conductivity of the electrode's solid phase, size of active-material particles in the electrode), cell design (heat transfer coefficient at the electrodes), and cell operation (discharge current density or C-rate) on both local thermal disequilibrium and the prediction accuracy of the thermal equilibrium approximation. We also applied our thermal model to a whole NMC battery with multiple units and evaluate its effectiveness by comparing the predicted and measured battery surface temperature. Our analysis leads to the following major conclusions.

- Our local thermal non-equilibrium model is self-consistent, i.e., it reduces to its equilibrium counterpart and yields commensurate predictions of internal temperature, when the electrolyte and the solid phase in porous electrodes are in local thermal equilibrium.
- Electrodes, whose solid phase has high thermal conductivity, operate close to the local thermal equilibrium under high C-rates. That is because the enhanced solid–electrolyte interfacial heat transfer ameliorates the heat generation non-uniformity between the two phases.
- Electrodes composed of larger solid particles are predicted to exhibit more pronounced local thermal disequilibrium. That is because of the longer characteristic time for thermal diffusion to eliminate the heat non-uniformity between the electrolyte and the solid.

Table 2
Identified parameters in the non-equilibrium-P2D and equilibrium-P2D models for the NMC battery.

	Non-equilibrium	Equilibrium
Maximum concentration in negative electrode, $c_{\text{smax,neg}}$ [mol/m^3]	32 638	32 778
Maximum concentration in positive electrode, $c_{\text{smax,pos}}$ [mol/m^3]	56 831	51 811
Negative electrode diffusivity at 25 °C, $D_{\text{s,neg}}$ [10^{-13}m^2/s]	1.36	3.16
Positive electrode diffusivity at 25 °C, $D_{\text{s,pos}}$ [10^{-14}m^2/s]	1.96	2.81
Negative reaction rate constant, $k_{0,\text{neg}}$ [10^{-13}m/s]	2.50	0.74
Positive reaction rate constant, $k_{0,\text{pos}}$ [10^{-12}m$^{2.5}$/s/mol$^{0.5}$]	0.72	9.51
Thermal conductivity of the casing, λ_{case} [W/m/K]	10.7	8.97

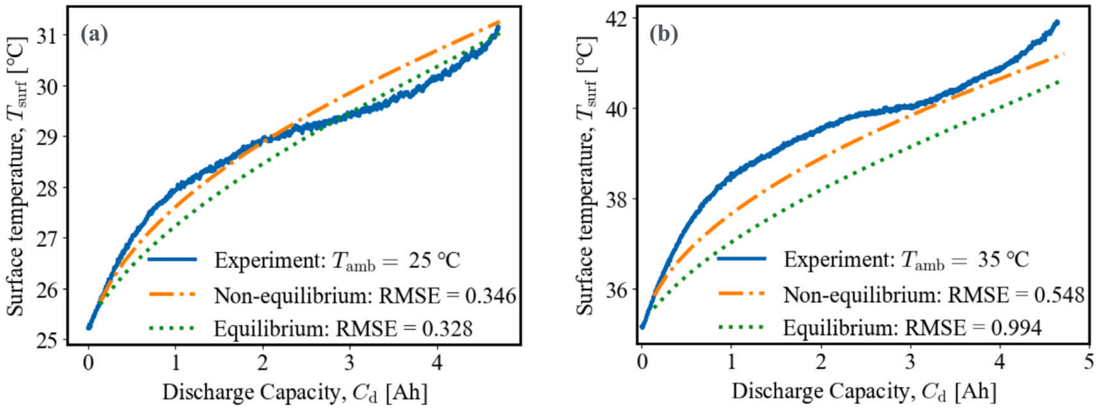

Fig. 8. Observed and predicted surface temperature of a cylindrical LG M50 cell during a 1C discharge test with (Left) 25 and (Right) 35 °C ambient temperature. The observational data are reported in [44]. The non-equilibrium and equilibrium models are parameterized for 25 °C, and are used in the purely predictive fashion for 35 °C.

- Enhanced cooling of a cell's surface decreases the cell's core temperature and slows down the cell's discharge, but increases the local thermal non-equilibrium due to the severe heat conduction non-uniformity between the two phases. That puts premium on non-equilibrium P2D models like ours.
- Large discharge current density (C-rate) aggravates the local thermal disequilibrium by increasing the discrepancy in heat generation within the two phases. The thermal-equilibrium approximation severely underestimates a cell's internal temperature, potentially undermining the battery's thermal management.
- Applied to a whole lithium battery with multiple units, the non-equilibrium model shows its effectiveness by the good agreement between the predicted and measured surface temperature, while the equilibrium model shows obvious temperature underestimation.

CRediT authorship contribution statement

Xiaoyu Yang: Writing – original draft, Visualization, Software, Methodology, Investigation, Formal analysis. **Weiyu Li:** Writing – review & editing, Methodology, Conceptualization. **Kimoon Um:** Writing – review & editing, Resources, Conceptualization. **Daniel M. Tartakovsky:** Writing – review & editing, Project administration, Methodology, Funding acquisition, Conceptualization.

Declaration of competing interest

The authors declare that they have no known competing financial interests or personal relationships that could have appeared to influence the work reported in this paper.

Data availability

No data was used for the research described in the article.

Acknowledgments

This work was supported in part by Hyundai Motor Group, Republic of Korea, by Air Force Office of Scientific Research, USA under award number FA9550-21-1-0381, and by StorageX at Stanford University, USA.

Appendix. Heat transfer in solid particles

When the solid phase of an electrode is treated as a continuum 1D medium, its temperature $T_{\text{s}}(x,t)$ is described in a manner similar to Eq. (6),

$$(1-\omega)\rho_{\text{s}}c_{\text{s}}\frac{\partial T_{\text{s}}}{\partial t} = \frac{\partial}{\partial x}\left(\lambda_{\text{s}}^{\text{eff}}\frac{\partial T_{\text{s}}}{\partial x}\right) + Q^{\text{s}}_{\text{ohm}} + A_{\text{rs}}Q^{\text{s}}_{\text{int}}, \qquad x \in (0,L), \qquad t > 0. \tag{A.1}$$

The first term on the right-hand-side of this equation represents heat conduction, the second is the solid Ohmic heat, and the last term denotes the interfacial heat entering the solid phase from the electrolyte. The local thermal equilibrium model (3a) assumes $T_{\text{s}} = T_{\text{e}} = T$, and is derived by combining Eqs. (A.1) and (6).

In the P2D framework, we use Eq. (6) to describe heat transfer in the electrolyte, but represent the solid phase at any position x via a non-overlapping spheres. The net through-cell conductive heat entering the solid and the solid Ohmic heat in these spheres are treated as uniformly distributed volumetric heat sources, and the radial heat conduction is also taken into account to describe the solid temperature $T_{\text{s}}(r;x,t)$ with the differential equation

$$\rho_{\text{s}}c_{\text{s}}\frac{\partial T_{\text{s}}}{\partial t} = \frac{1}{1-\omega}\frac{\partial}{\partial x}\left(\lambda_{\text{s}}^{\text{eff}}\frac{\partial T^{\text{e}}}{\partial x}\right) + \frac{Q^{\text{s}}_{\text{ohm}}}{1-\omega} + \frac{1}{r^2}\frac{\partial}{\partial r}\left(\lambda_{\text{s}}r^2\frac{\partial T_{\text{s}}}{\partial r}\right). \tag{A.2}$$

This equation is defined within the electrodes, $x \in (0, L_{\text{neg}}) \cup (L - L_{\text{pos}}, L)$; with $0 < r < R$ and $t > 0$. The temperature of the porous electrodes in the x direction is the same as the electrolyte temperature

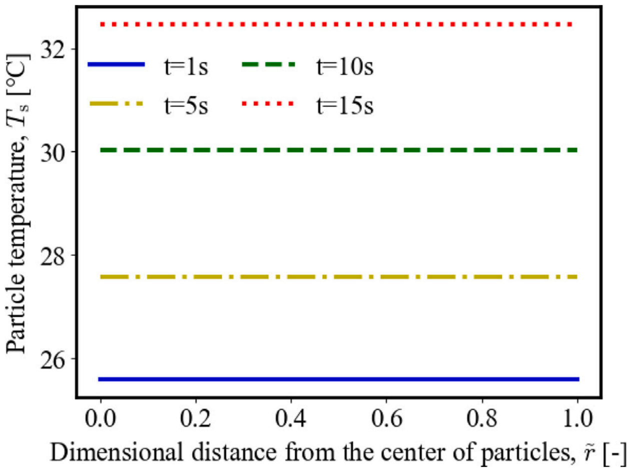

Fig. A.1. Radial distribution of the temperature of a solid particle, $T_s(r;x,t)$, located in the middle of the negative electrode in the synthetic LIB under local thermal equilibrium. The temperature is plotted against the dimensional distance from the particle's center $\tilde{r} = r/R$ and at different time.

T_e, so the contribution of through-cell heat conduction in the solid phase is described by T_e.

The local thermal equilibrium exists when the temperature within the solid particles is uniform, i.e., the last term in Eq. (A.2) vanishes,

$$\rho^\mathrm{s} c_\mathrm{p}^\mathrm{s} \frac{\partial T^\mathrm{s}}{\partial t} = \frac{1}{1-\omega} \frac{\partial}{\partial x}\left(\lambda_\mathrm{eff}^\mathrm{s} \frac{\partial T^\mathrm{e}}{\partial x}\right) + \frac{Q_\mathrm{ohm}^\mathrm{s}}{1-\omega}. \tag{A.3}$$

In that case, there is no heat entering solid phase from the solid/electrolyte interface, $Q_\mathrm{int}^\mathrm{s} = 0$, and Eq. (A.1) also reduces to Eqs. (A.3). Therefore, our local thermal non-equilibrium model and the 1D thermal model are consistent with each other under the local thermal equilibrium.

References

[1] M.-K. Tran, A. Mevawalla, A. Aziz, S. Panchal, Y. Xie, M. Fowler, A review of lithium-ion battery thermal runaway modeling and diagnosis approaches, Processes 10 (6) (2022) 1192.

[2] E. Tardy, P.-X. Thivel, F. Druart, P. Kuntz, D. Devaux, Y. Bultel, Internal temperature distribution in lithium-ion battery cell and module based on a 3D electrothermal model: An investigation of real geometry, entropy change and thermal process, J. Energy Storage 64 (2023) 107090.

[3] K. Shah, S.J. Drake, D.A. Wetz, J.K. Ostanek, S.P. Miller, J.M. Heinzel, A. Jain, An experimentally validated transient thermal model for cylindrical Li-ion cells, J. Power Sources 271 (2014) 262–268.

[4] S. Drake, M. Martin, D. Wetz, J. Ostanek, S. Miller, J. Heinzel, A. Jain, Heat generation rate measurement in a Li-ion cell at large c-rates through temperature and heat flux measurements, J. Power Sources 285 (2015) 266–273.

[5] Y. Kim, S. Mohan, J.B. Siegel, A.G. Stefanopoulou, Y. Ding, The estimation of temperature distribution in cylindrical battery cells under unknown cooling conditions, IEEE Trans. Control Syst. Technol. 22 (6) (2014) 2277–2286.

[6] R. Srinivasan, Monitoring dynamic thermal behavior of the carbon anode in a lithium-ion cell using a four-probe technique, J. Power Sources 198 (2012) 351–358.

[7] R.R. Richardson, P.T. Ireland, D.A. Howey, Battery internal temperature estimation by combined impedance and surface temperature measurement, J. Power Sources 265 (2014) 254–261.

[8] P. Wang, L. Yang, H. Wang, D.M. Tartakovsky, S. Onori, Temperature estimation from current and voltage measurements in lithium-ion battery systems, J. Power Storage 34 (2021) 102133, http://dx.doi.org/10.1016/j.est.2020.102133.

[9] X. Lin, H.E. Perez, J.B. Siegel, A.G. Stefanopoulou, Y. Li, R.D. Anderson, Y. Ding, M.P. Castanier, Online parameterization of lumped thermal dynamics in cylindrical lithium ion batteries for core temperature estimation and health monitoring, IEEE Trans. Control Syst. Technol. 21 (5) (2012) 1745–1755.

[10] M. Song, Y. Hu, S.-Y. Choe, T.R. Garrick, Analysis of the heat generation rate of lithium-ion battery using an electrochemical thermal model, J. Electrochem. Soc. 167 (12) (2020) 120503.

[11] W. Ai, L. Kraft, J. Sturm, A. Jossen, B. Wu, Electrochemical thermal-mechanical modelling of stress inhomogeneity in lithium-ion pouch cells, J. Electrochem. Soc. 167 (1) (2020) 013512.

[12] C.-F. Chen, A. Verma, P.P. Mukherjee, Probing the role of electrode microstructure in the lithium-ion battery thermal behavior, J. Electrochem. Soc. 164 (11) (2017) E3146.

[13] G. Wang, D. Kong, P. Ping, X. He, H. Lv, H. Zhao, W. Hong, Modeling venting behavior of lithium-ion batteries during thermal runaway propagation by coupling cfd and thermal resistance network, Appl. Energy 334 (2023) 120660.

[14] M. Doyle, T.F. Fuller, J. Newman, Modeling of galvanostatic charge and discharge of the lithium/polymer/insertion cell, J. Electrochem. Soc. 140 (6) (1993) 1526.

[15] S.G. Marquis, V. Sulzer, R. Timms, C.P. Please, S.J. Chapman, An asymptotic derivation of a single particle model with electrolyte, J. Electrochem. Soc. 166 (15) (2019) A3693.

[16] T.L. Kirk, C.P. Please, S.J. Chapman, Physical modelling of the slow voltage relaxation phenomenon in lithium-ion batteries, J. Electrochem. Soc. 168 (6) (2021) 060554.

[17] F. Boso, W. Li, K. Um, D.M. Tartakovsky, Impact of carbon binder domain on the performance of lithium-metal batteries, J. Electrochem. Soc. 169 (10) (2022) 100550.

[18] W. Li, H.A. Tchelepi, D.M. Tartakovsky, Screening of electrolyte-anode buffers to suppress lithium dendrite growth in all-solid-state batteries, J. Electrochem. Soc. 170 (5) (2023) 050510.

[19] Y. Ye, Y. Shi, N. Cai, J. Lee, X. He, Electro-thermal modeling and experimental validation for lithium ion battery, J. Power Sources 199 (2012) 227–238.

[20] L. Cai, R.E. White, An efficient electrochemical–thermal model for a lithium-ion cell by using the proper orthogonal decomposition method, J. Electrochem. Soc. 157 (11) (2010) A1188.

[21] K. Kumaresan, G. Sikha, R.E. White, Thermal model for a li-ion cell, J. Electrochem. Soc. 155 (2) (2007) A164.

[22] A. Lamorgese, R. Mauri, B. Tellini, Electrochemical-thermal P2D aging model of a LiCoO2/graphite cell: Capacity fade simulations, J. Energy Storage 20 (2018) 289–297.

[23] V. Esfahanian, F. Chaychizadeh, H. Dehghandorost, H. Shokouhmand, An efficient thermal-electrochemical simulation of lithium-ion battery using proper mathematical-physical cfd schemes, J. Electrochem. Soc. 166 (8) (2019) A1520.

[24] P.R. Nileshwar, A. McGordon, T. Ashwin, D. Greenwood, Parametric optimization study of a lithium-ion cell, Energy Procedia 138 (2017) 829–834.

[25] W. Li, D.M. Tartakovsky, Effective models of heat conduction in composite electrodes, J. Electrochem. Soc. 170 (10) (2023) 100503.

[26] A. Vadakkepatt, B. Trembacki, S.R. Mathur, J.Y. Murthy, Bruggeman's exponents for effective thermal conductivity of lithium-ion battery electrodes, J. Electrochem. Soc. 163 (2) (2015) A119.

[27] X. Zhang, D.M. Tartakovsky, Effective ion diffusion in charged nanoporous materials, J. Electrochem. Soc. 164 (4) (2017) E53.

[28] F.L.E. Usseglio-Viretta, A. Colclasure, A.N. Mistry, K.P.Y. Claver, F. Pouraghajan, D.P. Finegan, T.M.M. Heenan, D. Abraham, P.P. Mukherjee, D. Wheeler, Resolving the discrepancy in tortuosity factor estimation for Li-ion battery electrodes through micro-macro modeling and experiment, J. Electrochem. Soc. 165 (14) (2018) A3403–A3426.

[29] V. Sulzer, S.G. Marquis, R. Timms, M. Robinson, S.J. Chapman, Python battery mathematical modelling (PyBaMM), J. Open Res. Softw. 9 (1) (2021).

[30] F. Richter, S. Kjelstrup, P.J.S. Vie, O.S. Burheim, Thermal conductivity and internal temperature profiles of Li-ion secondary batteries, J. Power Sources 359 (2017) 592–600.

[31] F. Richter, P.J.S. Vie, S. Kjelstrup, O.S. Burheim, Measurements of ageing and thermal conductivity in a secondary NMC-hard carbon Li-ion battery and the impact on internal temperature profiles, Electrochim. Acta 250 (2017) 228–237.

[32] B. Yan, C. Lim, L. Yin, L. Zhu, Simulation of heat generation in a reconstructed LiCoO2 cathode during galvanostatic discharge, Electrochim. Acta 100 (2013) 171–179.

[33] Y. Ye, L.H. Saw, Y. Shi, K. Somasundaram, A.A.O. Tay, Effect of thermal contact resistances on fast charging of large format lithium ion batteries, Electrochim. Acta 134 (2014) 327–337.

[34] M. Ecker, T.K.D. Tran, P. Dechent, S. Käbitz, A. Warnecke, D.U. Sauer, Parameterization of a physico-chemical model of a lithium-ion battery: I. determination of parameters, J. Electrochem. Soc. 162 (9) (2015) A1836.

[35] D. Werner, A. Loges, D.J. Becker, T. Wetzel, Thermal conductivity of Li-ion batteries and their electrode configurations–a novel combination of modelling and experimental approach, J. Power Sources 364 (2017) 72–83.

[36] M. Meyer, L. Komsiyska, B. Lenz, C. Agert, Study of the local soc distribution in a lithium-ion battery by physical and electrochemical modeling and simulation, Appl. Math. Model. 37 (4) (2013) 2016–2027.

[37] E. Pohjalainen, T. Rauhala, M. Valkeapää, J. Kallioinen, T. Kallio, Effect of Li4Ti5O12 particle size on the performance of lithium ion battery electrodes at high C-rates and low temperatures, J. Phys. Chem. C 119 (5) (2015) 2277–2283.

[38] P. Wang, X. Zhang, L. Yang, X. Zhang, M. Yang, H. Chen, D. Fang, Real-time monitoring of internal temperature evolution of the lithium-ion coin cell battery during the charge and discharge process, Extreme Mech. Lett. 9 (2016) 459–466.

[39] R. Kantharaj, A.M. Marconnet, Heat generation and thermal transport in lithium-ion batteries: a scale-bridging perspective, Nanoscale Microscale Thermophys. Eng. 23 (2) (2019) 128–156.

[40] T.M. Bandhauer, S. Garimella, T.F. Fuller, A critical review of thermal issues in lithium-ion batteries, J. Electrochem. Soc. 158 (3) (2011) R1.

[41] S.-C. Chen, Y.-Y. Wang, C.-C. Wan, Thermal analysis of spirally wound lithium batteries, J. Electrochem. Soc. 153 (4) (2006) A637.

[42] X. Zhang, Thermal analysis of a cylindrical lithium-ion battery, Electrochim. Acta 56 (3) (2011) 1246–1255.

[43] L. Zhang, C. Lyu, G. Hinds, L. Wang, W. Luo, J. Zheng, K. Ma, Parameter sensitivity analysis of cylindrical LiFePO4 battery performance using multi-physics modeling, J. Electrochem. Soc. 161 (5) (2014) A762.

[44] E. Catenaro, S. Onori, Experimental data of lithium-ion batteries under galvanostatic discharge tests at different rates and temperatures of operation, Data Brief 35 (2021) 106894.

[45] C.-H. Chen, F.B. Planella, K. O'regan, D. Gastol, W.D. Widanage, E. Kendrick, Development of experimental techniques for parameterization of multi-scale lithium-ion battery models, J. Electrochem. Soc. 167 (8) (2020) 080534.

[46] K. O'Regan, F.B. Planella, W.D. Widanage, E. Kendrick, Thermal-electrochemical parameters of a high energy lithium-ion cylindrical battery, Electrochim. Acta 425 (2022) 140700.

[47] J. Blank, K. Deb, Pymoo: Multi-objective optimization in Python, IEEE Access 8 (2020) 89497–89509.